Heat and Mass Transfer
https://doi.org/10.1007/s00231-021-03097-8

ORIGINAL ARTICLE

Numerical investigation of expandable graphite suppression on metal-based fire

Ivan Miguel De Cachinho Cordeiro[1] · Hengrui Liu[1] · Anthony Chun Yin Yuen[1] · Timothy Bo Yuan Chen[1] · Ao Li[1] · Rui Feng Cao[1] · Guan Heng Yeoh[1,2]

Received: 18 December 2020 / Accepted: 2 June 2021
© The Author(s), under exclusive licence to Springer-Verlag GmbH Germany, part of Springer Nature 2021

Abstract

Aqueous suppression systems (i.e. fire sprinkler, water mist) have been extensively utilised for compartmental fire suppression due to their significant heat extraction ability. Nevertheless, challenges can be foreseen in suppressing water-reactive chemicals as a violent explosive reaction will be triggered, such as alkali metals (i.e. Na, Li) and alkali metal hydrides (i.e. LiH, $LiAlH_4$). In this study, expandable graphite (EG) is proposed as a potential suppressant against alkaline metal fire due to its advantageous thermal properties and chemical stability. In-house user-defined functions (UDFs) are developed to characterise the particle expansion coupled with the heat and mass transfer process between EG and the fluid mixture. The model is incorporated in the large eddy simulation (LES) framework to study the temporal fire behaviours and the suppression effect of EG against the flame plume. The numerical model was validated by comparison of temperature profiles and expansion rate of EG particles along the suppression event against experimental results. The EG was found to be relatively effective in fire suppression compared to the same amount of natural graphite. Parametric analysis was conducted on a range of EG particle size between 400 μm—1000 μm to investigate the suppression mechanisms and the suppression efficiency of EG particles against metal fires. Within the range of the current study (400 μm—1000 μm), the EG particle diameter of 400 μm has achieved the most effective suppression performance and the suppression time of 2 s. It is observed that the smaller size of EG tends to be effective in fire suppression than the larger sizes.

Nomenclature

A	Inlet Area (m2)
A_0	Initial Inlet Area (m2)
A_p	Surface Area of Particle (m2)
C_d	Drag Coefficient
C_s	WALE Model Constant
c_p	Heat Capacity (J/K)
D^*	Characteristic Length (m)
d	Distance to the Closest Wall (m)
d_p	Particle Diameter (m)
F	Additional Force (N)
f	Mixture Fraction
gi	Gravity (m/s2)
h	Convective Heat Transfer Coefficient (W/m2K)
L_s	Mixing Length for Sub-grid Scales
m_p	Mass of Particle (kg)
m_f	Mass Loss Coefficient (kg/s)
$\overline{p}$	Background Pressure (Pa)
Pr	Molecular Prandtl Number
Re	Reynold's Number
S_{ij}^d	Rate-of-Strain Tensor
$\overline{S_{rad}}$	Global Radiative Heat Exchange
$\overline{T}$	Temperature (K)
T_∞	Local Temperature of the Continuous Phase (K)
T_p	Particle Temperature (K)
V_0	Initial Volume (m3)
$\alpha_{1,2,3}$	Range Constants For Corresponding Reynolds Number
κ_d	Von Kármán constant
$\in_p$	Particle Emissivity
σ	Stefan-Boltzmann constant
θ_R^4	Radiation Temperature (K)
ρ	Density (kg/m3)
ρ_p	Particle Density (kg/m3)
u_i	Velocity Vector (m/s)

✉ Anthony Chun Yin Yuen
c.y.yuen@unsw.edu.au

[1] School of Mechanical and Manufacturing Engineering, University of New South Wales, Sydney, NSW 2052, Australia

[2] Australian Nuclear Science and Technology Organization (ANSTO), Locked Bag 2001, Kirrawee DC, NSW 2232, Australia

Published online: 19 June 2021

u	Fluid Phase Velocity (m/s)
u_p	Particle Velocity (m/s)
μ	Molecular Viscosity (kg/ms)
μ_t	Turbulent Viscosity (kg/ms)
$\overline{\omega_T}$	Filtered Heat Release Rate (W)
δ_{ij}	Rate of Strain
τ_{ij}	Subgrid-scale Stress

1 Introduction

Metal-based compounds (i.e. magnesium-based hydrides, sodium alanates, lithium and potassium alanates, lithium nitrides, lithium boro- and beryllium hydrides, and intermetallic compounds) are generally recognised as hazardous and are required to be stored in a well-contained, temperature-controlled environment. This is due to the fact that most of the metal alloys are combustible metal powders with associated fire and explosion hazards before the hydride reaction [1]. According to the NFPA 484 [2], fire and explosion protection guidelines recommends special precautions associated with the handling of pyrophoric and water-reactive metal dust (i.e. CCPS Guidelines—1995; DOE Primer for Pyrophoric Materials – 1994) [3, 4]. Nonetheless, aqueous suppression agents, halogenated agents and carbon dioxide are inappropriate to be metal fire suppression agent, as most of the hydrides are water-reactive and undergo violent decomposition reaction with halogens and oxides. Therefore, a series of dry powders have been proposed as Class D fire suppression agents (i.e. Sodium chloride, graphite, copper powder, dry sand) [4], which specifically designed for combustible metal fire suppression. However, high agent mass ratio, environment contamination and lack of reigniting prevention in disturbed pool bed were also observed in sodium chloride and graphite against sodium fire [5, 6].

Expandable graphite (EG) is an advanced graphite intercalation compound (GIC), which is prepared by implementing non-carbonaceous atoms or molecules into graphite's carbon layers [7], this process can be accomplished through chemical, electrochemical and mechanical reaction [8]. Afterwards, the inter-layer distance of EG is increased as the binding force between graphite layers is diminished [9], EG hence becomes "expandable" since the van der Waal's between graphite layers can be broken by heat energy, while the covalent bond between carbon atoms will retain the carbon hexagonal ring of each single layer [10]. In the expansion process, EG particles will be expanded 100 – 300 times in volume, the expansion rate can be varied between different expansion temperature and preparation approaches [11]. The expansion characteristics of EG has led to its extensive application in flame retardancy [12–15], sealing technology [16], phase change material (PCM) [17] and adsorption material [18]. EG is possessed of several characteristics that are superior in flame retardancy application: i) high thermal resistance; ii) non-toxicity; iii) non-dripping; iv) low smoke yield and v) high chemical stability [19]. To study these physical behaviours, a comprehensive numerical model would be a viable option to consider the fully coupled and interacting effect between EG and the fluid mixture.

Computational fluid dynamics (CFD) is an effective tool for practical fire simulations including bushfires, compartment fires, and more fundamental pyrolysis and combustion problems. Recently, the large eddy simulation (LES) approach was found to be advantageous for the prediction of time-dependent flaming behaviours due to its capability in considering the temporal fluctuating behaviours led by turbulence/fuel-mixture interaction [20, 21], the LES has also revealed its potential in multiphase flow problem [22]. On the other hand, the discrete phase model (DPM) was an effective tool to track/trace particles and couple the effect against the fluid component in the control element. This technique was recently utilised in the assessment of fire suppression systems for water-mist and sprinklers. For instance, Liu et al. [23, 24] studied the effect of various water droplet sizes in fire sprinkler and water mist system and Li et al. [25] conducted a series of model scale tunnel fire suppression by utilizing DPM method to simulate the water spray from fire sprinklers. Li et al. [26] have optimized parameters such as particle sphericity and micron sizes for abrasive particles under turbulent multiphase flow. Yan et al. [27] have discovered that the Eulerian–Lagrangian approach has obvious advantage in modelling particle–wall interactions. However, the current DPM models are limited in consideration of inert particle expansion. Therefore, for the purpose of studying the EG suppression system, it is necessary to develop a new model to bridge the missing knowledge.

In this study, EG is proposed as an effective suppressant in alkaline metal fire suppression. The effectiveness of EG particles against a sodium-based fire has been studied numerically for the first time, by utilising a coupled in-house UDF model with the LES framework. The following are the objectives of this study:

a) Establish an experimentally validated EG suppression model, where the gas-phase turbulent reacting gas mixture model coupled with an advanced discrete phase model (DPM), to simulate the heat and mass transfer between particles and fire, the time-dependent movement of expandable particles were also tracked.
b) By compiling multiple User-Defined Functions (UDFs), the temperature-dependent volume expansion of EG has been replicated according to conducted experiments. The "barrier effect", which affecting fuel surface area has also been simulated and validated with experimental results.

c) Conduct parametric studies between natural graphite and various size of EG, the temperature profiles and expansion rate against time and temperature were compared and the suppression efficiency of each case is revealed. The suppression mechanisms of various sizes of EG against metal fires are also analysed through the temperature distribution contour.

2 Mathematical models

Computational Fluid Dynamic (CFD) modelling is an effective approach to replicate the complex heat and mass transfer behaviour between the suppression agents and the fire, and was proven to be reliable for practice fire suppression simulation studies [23, 28]. To investigate the feasibility of expandable particles suppression system for metal fire, Large Eddy Simulation (LES) approach incorporating sub-grid scale (SGS) turbulence models coupled with non-premixed combustion and a set of user-defined functions (UDFs) were constructed to describe the fire phenomena interacting with expandable inert particles. The current approach is practical for fire modelling since the temporary fluctuation behaviour of the flame can be coupled to the other sub-modelling components [29, 30].

2.1 Favre-filtering governing equations

The transport equation of fluid flow in LES approach is described by the fundamental conservation equations for Newtonian fluid. Favre-filtering approach is introduced to describe the conservation of mass, momentum, and energy. Low Mach number assumption was also suggested for turbulent fire simulations [31, 32].

$$\frac{\partial \rho}{\partial t} + \frac{\partial (\rho \bar{u}_i)}{\partial x_i} = 0 \tag{1}$$

$$\frac{\partial \rho \bar{u}_i}{\partial t} + \frac{\partial \rho \bar{u}_i \bar{u}_j}{\partial x_j} = \frac{\partial}{\partial x_j}\left[\mu\left(\frac{\partial \rho \bar{u}_i}{\partial x_j} + \frac{\partial \bar{u}_j}{\partial x_i}\right) - \frac{2}{3}\mu \frac{\partial \rho \bar{u}_k}{\partial x_k}\delta_{ij}\right] - \frac{\partial \bar{p}}{\partial x_i} - \frac{\partial \tau_{ij}}{\partial x_j} \tag{2}$$

$$\frac{\partial \rho C_p \bar{T}}{\partial t} + \frac{\partial \rho \bar{u}_i C_p \bar{T}}{\partial x_i} = \frac{\partial}{\partial x_i}\left(\frac{\mu C_p}{Pr}\frac{\partial \bar{T}}{\partial x_i}\right) - \frac{\partial \tau_{ij}}{\partial x_i} + \bar{\omega_T} + \bar{S_{rad}} \tag{3}$$

where ρ is density, $\bar{u}_i$ is the velocity vector, $\bar{p}$ is the pressure, μ is the dynamic viscosity, C_p is the specific heat, $\bar{T}$ is the temperature, δ_{ij} and τ_{ij} are the rate of strain tensor and subgrid-scale stress respectively. For the energy equation, Pr is the molecular Prandtl number, $\bar{\omega_T}$ represents the filtered heat release rate and $\bar{S_{rad}}$ denotes the global radiative heat exchange.

2.2 Turbulence model

The effectiveness of LES models is contributed by the implementation of Subgrid-scale (SGS) models, where complex turbulent flows are resolved under limited meshing quality with considerable accuracy. To resolve the high turbulence fluctuation of the fire, the SGS model was introduced by employing the Boussinesq hypothesis [33]. Wall-Adapting Local Eddy-viscosity (WALE) model established by Nicoud and Ducros [34] was applied to enhance the accuracy of the LES model on resolving turbulent flame [21, 35, 36]. The turbulent viscosity is formulated as:

$$\mu_t = \rho L_s^2 \frac{\left(S_{ij}^d S_{ij}^d\right)^{\frac{3}{2}}}{\left(\overline{S_{ij}S_{ij}}\right)^{\frac{5}{2}} + \left(S_{ij}^d S_{ij}^d\right)^{\frac{5}{4}}} \tag{4}$$

In WALE SGS model, the mixing length for sub-grid scales L_s and rate-of-strain tensor S_{ij}^d are defined as:

$$L_s = \min(\kappa d, C_s \Delta) \tag{5}$$

$$S_{ij}^d = \frac{1}{2}\left(\left(\frac{\partial \bar{u}_i}{\partial x_j}\right)^2 + \left(\frac{\partial \bar{u}_j}{\partial x_i}\right)^2\right) - \frac{1}{3}\delta_{ij}\left(\frac{\partial \bar{u}_k}{\partial x_k}\right)^2 \tag{6}$$

where the WALE model constant C_s is suggested to be 0.5 [34], Δ is the sub-grid length scale where $\Delta = \left(\delta_x \delta_y \delta_z\right)^{\frac{1}{3}}$, κ and d are the von Kármán constant and distance to the closest wall respectively.

2.3 Non-premixed combustion model

To characterize the combustion behaviour, non-premixed combustion model was adopted to replicate a similar heat release profile from the original experiment. In the non-premixed modelling approach, fuel and oxidisers were governed by the mixture fraction and achieved chemical equilibrium by applying the Steady Laminar Flamelet model. In the LES model, the transport equation of the mixture fraction is defined as:

$$\frac{\partial}{\partial t}\left(\rho \bar{f}\right) + \nabla \cdot \left(\rho v \bar{f}\right) = \nabla \cdot \left(\frac{u_t}{\sigma_t}\nabla \bar{f}\right) \tag{7}$$

where the mixture fraction variance $\bar{f'^2}$ is defined as:

$$\bar{f^{2}} = 0.5 \times L_s^2 \left|\nabla \bar{f}\right|^2 \tag{8}$$

The chemical reaction process would be described by the beta function probability density function (PDF) approach, which governs the fluctuation of the mixture fraction and level of strain rate in a form of probability density [37].

2.4 Discrete phase inert particle model

The modelling of expandable particles has been a complex problem as various physical phenomena are involved, such as heat expansion and residuals modelling, which lead to a more complex heat and mass exchange between particles and flame plume. The reflection of expandable particles' suppression effect in the current study is achieved by implementing multiple UDFs. Figure 1 illustrates the schematic framework and logical flow of the UDF code that governs particle expansion, particle sampling and inlet area control.

2.4.1 Particle motions

The trajectory of discrete phase particles is predicted by governing force conservation in Lagrangian frame, under spherical drag model [38]. The force balance can be interpreted as:

$$\frac{du_p}{dt} = \frac{3\mu C_D Re}{4\rho_p d_p^2}\left(u - u_p\right) + \frac{g_i(\rho_p - \rho)}{\rho_p} + F_i \tag{9}$$

where u and u_p is the fluid phase and particle velocity, μ is molecular viscosity, Re is the relative Reynolds number, ρ_p and d_p are density and diameter of the particle, force term F_i is the additional force involving Thermophoretic force, Brownian force, Saffman's Lift force. C_D is the drag coefficient for the spherical drag law which can be described as:

$$C_D = \alpha_1 + \frac{\alpha_2}{Re} + \frac{\alpha_3}{Re^2} \tag{10}$$

where $\alpha_1, \alpha_2, \alpha_3$ are the range constants for the corresponding Reynolds number.

2.4.2 Inert heat transfer

The fundamental heat transfer effect of the particles is governed by the Inert Heating Law until the particle reaches the corresponding vaporization temperature [39]. In the current application, since the vaporisation temperature of graphite is exceptionally high[40, 41], the inert heating law has dominated the heat transfer effect of the EG:

$$m_p c_p \frac{dT_p}{dt} = hA_p\left(T_\infty - T_p\right) + \epsilon_p A_p \sigma(\theta_R^4 - T_p^4) \tag{11}$$

where, m_p is the mass of the particle, c_p is the heat capacity, T_p is the particle temperature, h is the convective heat transfer coefficient, A_p is the surface area of the particle, T_∞ is the local temperature of the continuous phase, $\epsilon_p A_p \sigma(\theta_R^4 - T_p^4)$ is the radiation term of the particle, where ϵ_p is particle emissivity, σ is Stefan-Boltzmann constant,θ_R^4 is radiation temperature. Subsequently, the heat transfer effect between expandable particles and the flame plume is established in both conduction, convection and radiation. To obtain the

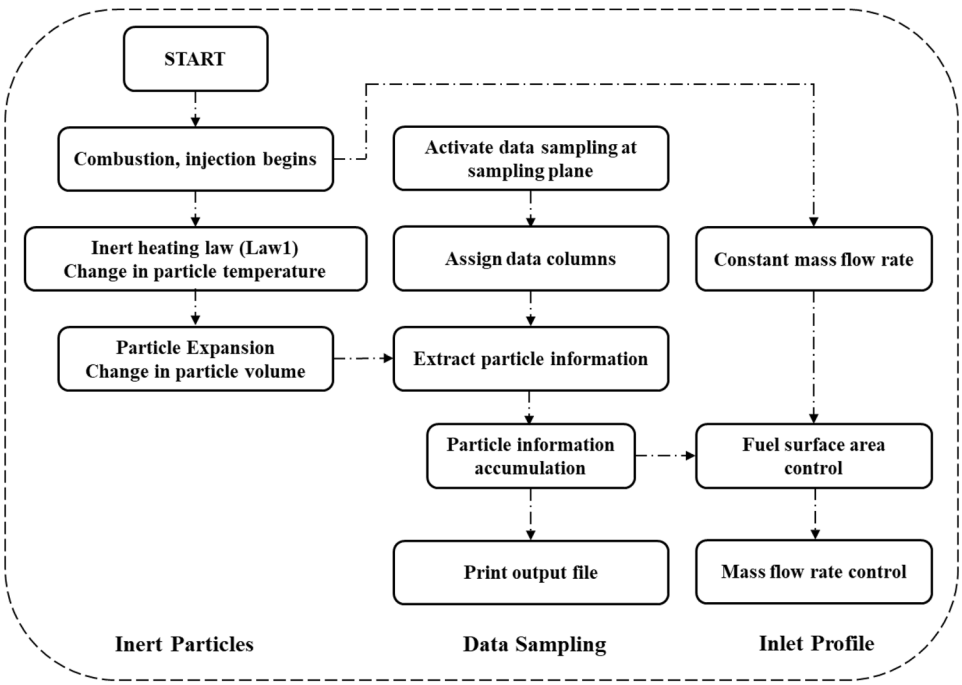


Fig. 1 Schematic Framework and Logical Flow of the UDF Code

linearized equation, the heat transfer equation can be integrated as follow:

$$m_p c_p \frac{dT_p}{dt} = A_p[-\left(h + \epsilon_p \sigma T_p^3\right)T_p + \left[hT_\infty + \epsilon_p \sigma \theta_R^4\right]] \quad (12)$$

Therefore, the particle temperature at the next time step can be predicted after the particle trajectory is calculated, where Δt is the integration time step:

$$T_p(t + \Delta t) = \alpha_p + \left[T_p(t) - \alpha_p\right]e^{-\beta_p \Delta t} \quad (13)$$

$$\alpha_p = \frac{hT_\infty + \epsilon_p \sigma \theta_R^4}{h + \epsilon_p \sigma T_p^3(t)} \quad (14)$$

$$\beta_p = \frac{A_p(h + \epsilon_p \sigma T_p^3(t))}{m_p C_p} \quad (15)$$

2.4.3 Particle expansion

The volume expansion of EG in the heat process has been observed in a series of experiment [43–45]. In order to replicate the heat expansion phenomenon of EG, a temperature-dependent function to alter particles' volume is essential, the expansion ratio of expandable particles with respect to change of temperature can be determined by experiments [9, 46, 47]. The experimental results are linearized into a power relationship through the MATLAB curve fitting tool. Nonetheless, this numerical approach possesses limitations similar to kinetics parameters optimization studies [48], where the numerical curve fitting scheme is semi-empirical and highly dependent on the adopted data set. The expansion function is biased towards the experimental conditions and material intrinsic properties, the experimental error will hence carry towards the numerical model. Therefore, to optimize the expansion characterization approach, three sets of experimental data were also adopted into the function and compared through the result of the simulation. It can be observed that three cases shared a similar trend of expansion rate against various temperature in Fig. 2. Figure 3 reveals the temperature profile of the thermocouple 0.05 m above the fuel surface while a different expansion function is adopted. Since three cases shared similar suppression performance, the experimental result from Case I was adopted into the expansion function due to its wide range of measured temperature, where the temperature was measured from 370 to 1270 K, while Case II and III measured 570 K to 1270 K only. Subsequentially, the expanded volume of each expandable particle can be predicted from the heat conducted to each particle, thus volume expansion would occur in the suppression event, while the particles are travelling through the flame plume (Table 1).

$$Expanded\ Volume\ \left(mLg^{-1}\right) = (-8.276 \times 10^9) \times T_p^{-2.784} + 513.2 \quad (16)$$

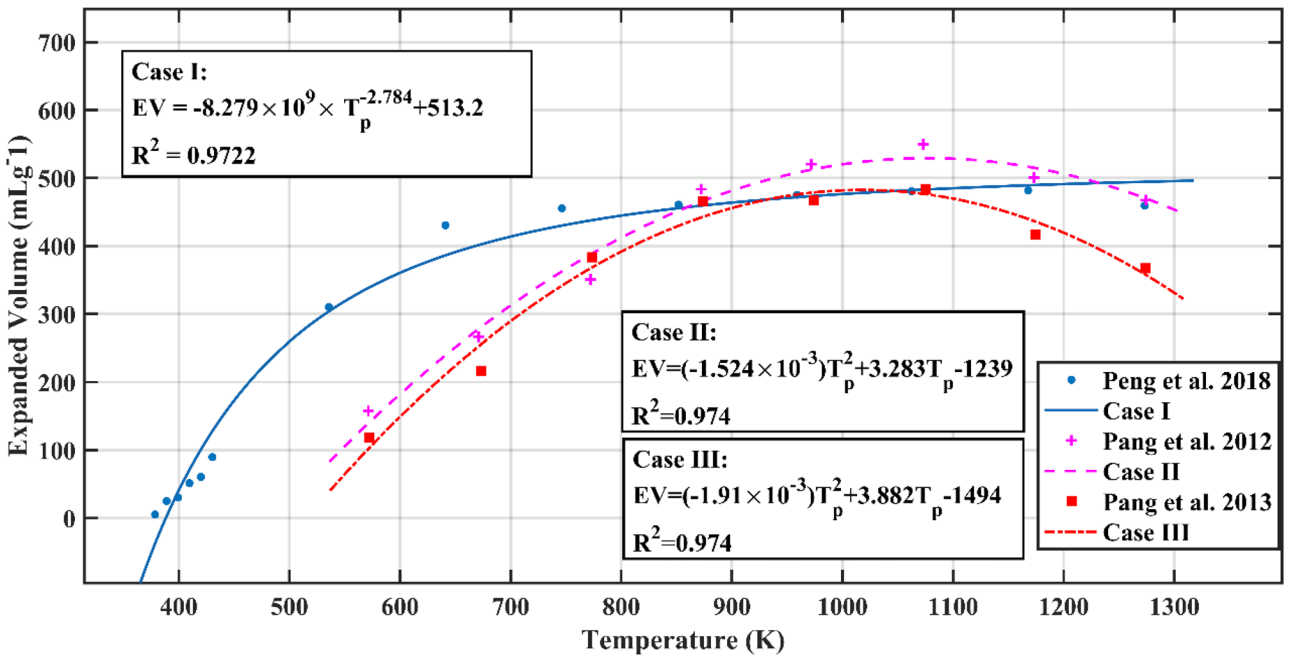


Fig. 2 Expanded Volume of against temperature according to conducted experiments

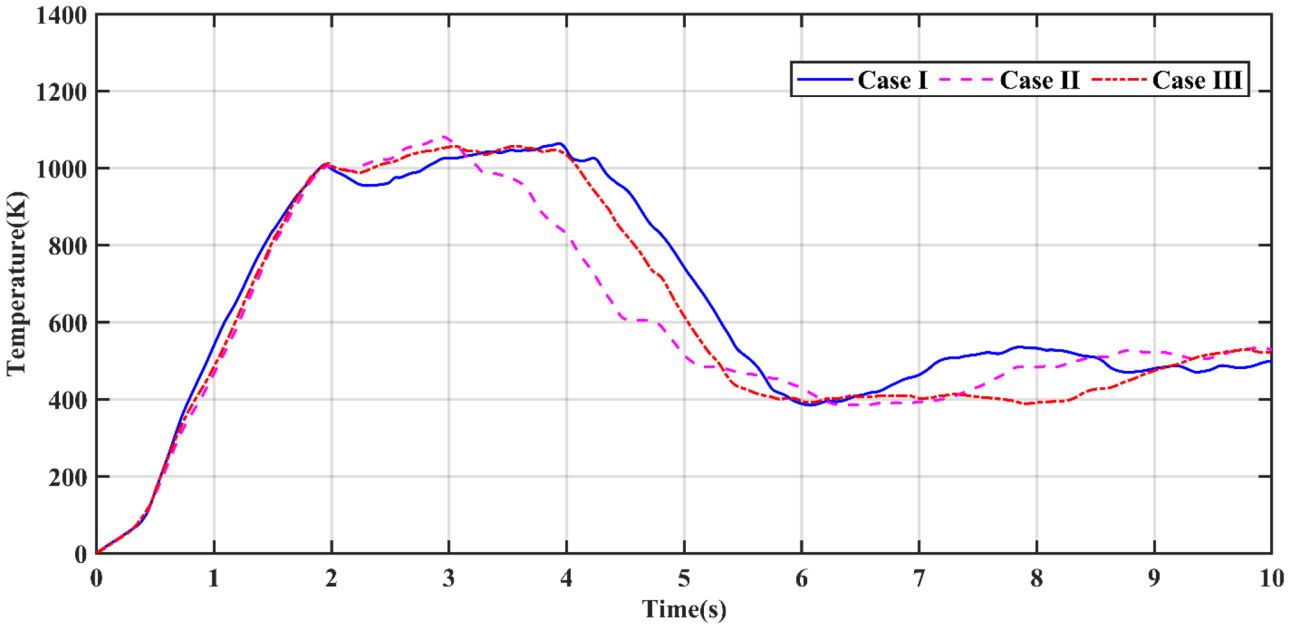


Fig. 3 Comparison of temperature profiles between adopted experimental results

2.4.4 Particle sampling

The extraction of particle information (i.e. particle temperature, diameter, mass, travel duration etc.) is vital for particle investigation, the second adopted UDF is used for the discrete phase sampling for ejected particles. The sampling algorithm will be executed for each particle arrival on the fuel surface for further processing. Since each ejected particle is assigned with a unique particle ID, the UDF is able to sample and extract all the particle information details, this information will be printed to an output script in a statistical approach. The total amount of the particles arrived at the fuel surface at each timestep can be sampled including all the real-time parameters, such as instant temperature, volume and velocity etc. These accumulated particles' information will govern the fuel inlet's condition to replicate graphite's barrier effect. Furthermore, the detailed particle sampling script also provides a solid approach to conduct particle analysis in the result section.

2.4.5 Barrier effect

$$\sum A = A_0 - \sum \left\{ \frac{3}{4} \left[m_p \times EV \right] \left(\frac{3\left[m_p \times EV \right]}{4\pi} \right)^{-\frac{1}{3}} \times \frac{m_f}{\rho_p} \right\} \tag{17}$$

$$\dot{m}_i = \dot{m}_a \times \sum A \tag{18}$$

It is suggested that the EG particles suppress the fire through heat transfer and suffocation[11, 49, 50]. While the particles were sprayed onto the fuel surface, the particles would absorb the heat from the flame and form a pile of powder after the expansion, where oxygen insulation occurs. Although the heat transfer effect can be replicated through the DPM heating law and swelling effect, the "barrier effect" is challenging to be replicated as the discrete phase particles will not interfere with the fluid mixture in terms of volume. Nonetheless, since the non-premix combustion model is utilised, where the fuel and oxidisers were governed by the mixture fraction and achieved chemical equilibrium through a vertically upward mass flow inlet, the "barrier effect" can be achieved by utilizing an "area control" to the fuel inlet. In this research, a novel approach has been made to replicate the "barrier effect" through particle sampling and inlet profile governing. After the expanded volume was calculated for each particle, the area of each particle will be accumulated through particle sampling at every timestep, the area of the fire inlet will be eventually controlled through the accumulated particle area, as the expanded graphite barrier is formed onto the fuel surface. Where $\sum A$ is the total area of the fire inlet, A_0 is the initial area, d_p is the diameter of the particle, m_f is the mass loss coefficient based on conducted thermogravimetric analysis [9, 49], ρ_p is the density of the particle.

3 Numerical configuration

3.1 Geometry and configuration

Figure 4 demonstrates the schematic layout and dimension of the numerical domain. The dimension of the numerical domain was configurated at 0.5 m × 0.5 m × 0.3 m, where

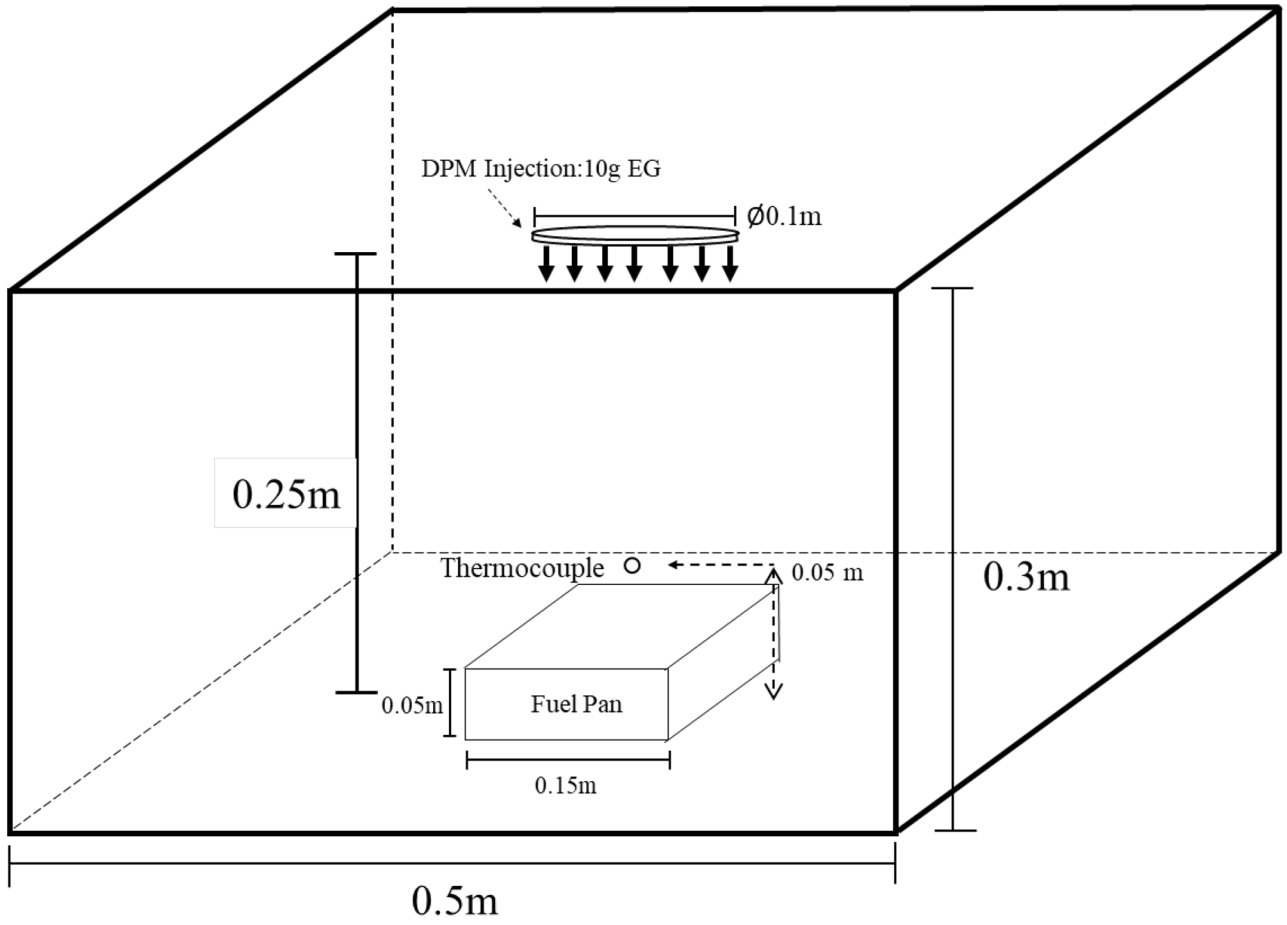


Fig. 4 Schematic Layout of Numerical Domain and DPM Injection

escape boundary conditions were set at the surrounding walls, ceiling, and floor for DPM parcels. Similar to the original experiment conducted by Ni et al. [49], a fuel crucible was configurated at the centre of the domain, with a dimension of 0.15 m × 0.15 m × 0.05 m, where a UDF-coupled fuel inlet was configurated at the upward surface of the fuel pan. On the other hand, the DPM injection was implemented with a diameter of 0.1 m, where 11 g of characterized EG particles was injected within 2 s. The thermophysical properties of EG were characterised through the coupled-UDF, including heat expansion and pyrolysis. A thermocouple was also configurated at the centre with 0.05 m above the floor along the y-axis. Table 2 presents the detailed configuration for both the boundary conditions of mixture fluid and DPM properties. The parameters for both fuel inlet and DPM injection were calculated based on the consumption statistics of the original experiment. Owing to the modelling limitation, it is challenging to completely replicate the pyrolysis mechanism and oxidation reaction of the actual metallic sodium fire in the original experiment. Nonetheless, since EG possesses high chemical stability, the chemical reaction between sodium and graphite is not considered in the model. Therefore, the heat and mass transfer nature of the sodium fire can be

Table 1 References of EG experimental data from previous literature studies

	Case I	Case II	Case III
Agent	Expandable Graphite		
Preparation solution	$KMnO_4$ and NH_4NO_3, $HClO_4$	$KMnO_4$, $Na_4P_2O_7$ and H_2SO_4	$KMnO_4$, HAc and H_2SO_4
Initiation Temperature (°C)	150	300	160
Reference	Peng et al. [9]	Pang et al. [11]	Pang et al. [42]

Table 2 Summary of Numerical Configuration

Numerical Domain Configuration		DPM Injection Parameters	
Domain Dimension (m)	$0.5 \times 0.5 \times 0.3$	Initial particle diameter (μm)	700
Fuel Inlet Area (m^2)	0.0225	Total agent mass (kg)	0.011
Mass Flow Rate per unit area (kg/s m^2)	3.69×10^{-3}	Injection duration (s)	2
Thermocouple Location	0.05 m above fuel surface	Injection plate radius (m)	0.05
Injection Location (m)	0.2 m above fuel surface	Initial volume (m^3)	1.80×10^{-10}
		Particle density (kg/m^3)	2200

replicated by configuring a non-premix methane combustion model, the fire characteristics of sodium fire were also validated in the validation section.

Table 3 demonstrated the parametric study conducted in this research, case 3 was configurated as a baseline model and validated from conducted experiments. To further investigate, case 2 & 3 would compare the suppression efficiency between EG and natural graphite flakes under the same amount of agent applied, where Case 2 is configurated with 11 g of natural graphite flakes. Case 1 would investigate the required amount of natural graphite to achieve suppression, the injection will be terminated once the suppression is achieved. Furthermore, to investigate the size parameters effect of EG, Case 3 – 7 conduct parametric studies on the suppression performance difference between various particle sizes of EG, where the diameter range between 400 μm—1000 μm will be investigated since Focke et al. demonstrated that this is the typical particle size range of EG [51]. The particle diameter in case 4 – 7 was configurated as 400 μm, 550 μm, 850 μm and 1000 μm to investigate the size spectrum.

3.2 Mesh independence

According to the characteristic length analysis suggested by DiNenno et al.[52], the meshing criteria for the simulation can be determined in the equation below, where D^* is the characteristic length, considering the heat release rate Q, density ρ_∞, specific heat c_p and the ambient temperature T_∞ of the air.

$$D^* = \left(\frac{\dot{Q}}{\rho_\infty c_p T_\infty \sqrt{g}} \right)^{\frac{2}{5}} \tag{19}$$

In order to demonstrate the verification of the proposed fire model, the total mass flow rate of the fire inlet along the suppression event was utilised for comparison between three mesh systems, which are Coarse (220,222 cells), Medium (640,144 cells), Fine (878,396 cells). Figure 5 presented an average converged result where the medium mesh (640,144 cells) achieved convergence to the fine mesh (878,396) with a lower computational cost. Therefore, the medium mesh was adopted for further numerical studies, where 640,144 uniform tetrahedral cells were applied for the mesh.

3.3 Validation

Prior to any particle injection, a "free burning" simulation was calibrated to extract the identical fire characteristics from the experiment. In the original experiment, 5 g of metallic sodium fuel was ignited and developed a metal fire where the temperature was maintained between 900 K – 1100 K for approximately 60 s. To achieve an identical heat release profile in numerical approach, the non-premixed combustion model was adopted and established a methane fire with a similar temperature profile for 60 s. For the sake of computational cost and the stability of the turbulence structure, instead of modelling the incipient and decay stage of the fire, the combustion model was calibrated to achieve the corresponding heat release rate in the 60 s

Table 3 Summary of parametric studies

Methane Fire	Case 1	Case 2	Case 3 (Exp)	Case 4	Case 5	Case 6	Case 7
Agent	Non-Expandable Graphite		Expandable Graphite				
Injected Agent Mass (kg)	0.275	0.011					
Injection Duration (s)	50	2					
Initial Particle diameter (μm)	700			400	550	850	1000
Initial volume (m^3)	1.80×10^{-10}			3.35×10^{-11}	8.71×10^{-11}	3.22×10^{-10}	5.24×10^{-10}
Number of Particles	720,000	30,000	30,000	130,000	52,000	14,000	9000

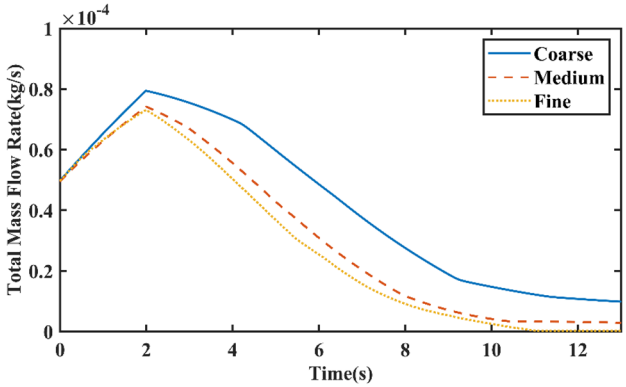


Fig. 5 Comparisons of the mass flow rate for coarse, medium and fine meshes

fully developed fire phase from the experiment, the simulation profile hence differs from the experiment in the time intervals of 0 s – 10 s and 70 s – 80 s. Nonetheless, it can be observed that the temperature predictions were in good agreement with the experimental result. Except for the "free burning" validation above, the temperature profiles and expansion rates of the suppression cases were also compared to the experimental results in the next section (Fig. 6).

4 Result and discussion

Table 4 summarized the result of the parametric study between natural graphite and various particle sizes of EG, under a limited amount of agent supply (11 g), EG in case 3 has successfully conduct suppression on 5 g metallic fuel fire, while natural graphite in case 2 did not effectively suppress the fire. Case 1 estimated the required amount of natural graphite to achieve suppression on the identical fire, 275 g of natural graphite was injected to achieve a steady low-temperature profile. Moreover, case 3 – 7 conducted parametric studies on the suppression performance difference between various particle sizes of EG, where the diameter range between 400 μm—1000 μm were investigated. The 400 μm EG in case 4 has demonstrated the most effective suppression among all the cases, the metal-based fire was extinguished within 2 s. The results will be analysed in the following section:

4.1 Validation of the benchmark case for the temperature profile

Figure 7 depict the temperature profile obtained from the thermocouple at 0.05 m above the fuel surface, for the purpose of capturing the various stages of the flame. Case 3 configuration is based on an experimental setup of Ni et al. [49]. Based on the validation results, it can be seen that the numerical predicted temperature profile is in good agreement with the experimental data. The relative overall difference is less than 5%. It should be noted that Case 3 utilised the proposed expansion model for EG, and it further evidenced that the model is capable of capture the expansion and suppression behaviours of the droplet particle against the active flame.

4.2 Influence of the expansion behaviour towards the temperature profile

Figure 8 reveals the comparison of temperature profile between case 2 and case 3, where the profile was measured at 0.05 m above the fuel surface, the results were also compared against experimental result for validation. Both case 2 and case 3 were configurated with identical mass, size and injection duration of the suppression agent compare to the experiment, yet case 2 utilized non-expandable graphite as a suppressant, while case 3 utilized EG. Free burning of 2 s was allowed to obtain a fully developed and stabilized fire

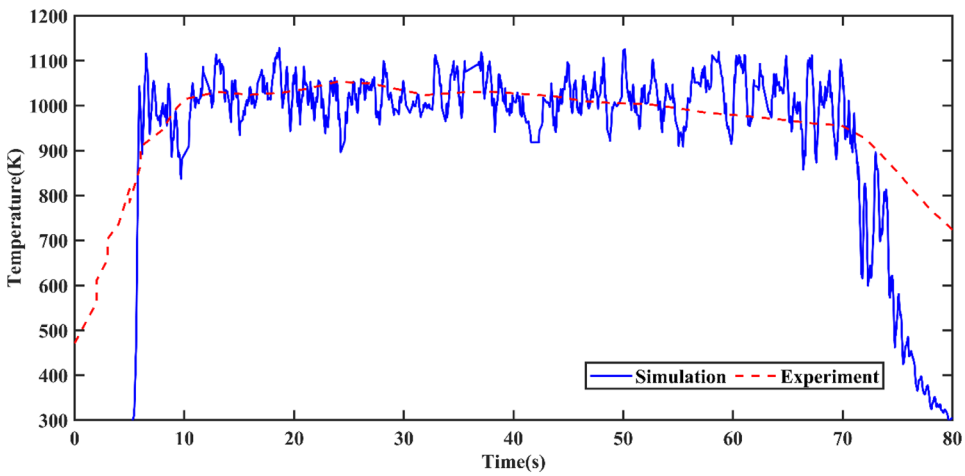


Fig. 6 Validation of the temperature profile at the free burning case

Table 4 Summary of conducted parametric studies' result

Methane Fire	Case 1	Case 2	Case 3 (Exp)	Case 4	Case 5	Case 6	Case 7
Suppression condition and duration	Y (48 s)	N	Y (4 s)	Y (2 s)	Y (2.5 s)	N	N

before the EG particles were released for all cases. In case 3, a temperature reduction from around 1000 K to around 450 K between t = 3.8 and t = 4.2 s, which can be attributed to the arrival of the expanded particles, covering the fuel surface and replaces the volume of the combustion mixture instantly. The injection has been terminated after 11 g of EG have been completely sprayed. On the other hand, the same amount of non-expandable graphite failed to conduct any form of suppression, as shown in case 2.

4.3 Effectiveness of expandable particles against non-expandable

On the other hand, Fig. 9 demonstrates the comparison of temperature profile between case 1 and case 3. In order to investigate the suppression performance differences between EG and natural graphite, case 1 simulated a non-expandable graphite suppression with unlimited agent mass provided. Without any volume expansion, 275 g of graphite was sprayed onto the fuel surface in order to reach the steady-state temperature profile at about 600 K in 48 s. In comparison, case 1 consumed 250 times more suppression agent than case 3, the poor suppression performance of case 1 and case 2 is ascribed to the limited fuel surface coverage, the graphite did not effectively reduce the reaction rate between fuel and oxygen. While in case 3, EG particles expanded at the fuel surface, which formed a compact pile of charring and diminished the contact area between fuel and oxygen.

4.4 Parametric study of various EG particle sizes

The initial diameter of EG is also a key parameter to be investigated. Figure 10 demonstrates the comparison of temperature profile obtained from case 3 to case 7. Among the cases studied, case 4 with 400 µm EG particles have achieved the best suppression performance, with the fire extinguished by 11 g of EG within 2 s. On the other hand, larger EG particles (case 6 with 850 µm and case 7 with 1000 µm) have demonstrated a relatively poor suppression performance that is similar to the natural non-expandable graphite flakes. Since the total amount of EG released for all the cases studied are equal, the ones with smaller initial sizes (i.e. 400 µm, 550 µm) naturally possess a larger quantity of particles. Several studies have outlined the relationship between particle size, the bulk density and porosity of the powder piles, although larger particles with lesser specific surface were suggested to decrease the porosity of tapped samples in confined space, smaller particles in practical scenario could increase bulk density and occupy the voids between the larger particles [53–55]. In case 4 and case 5,

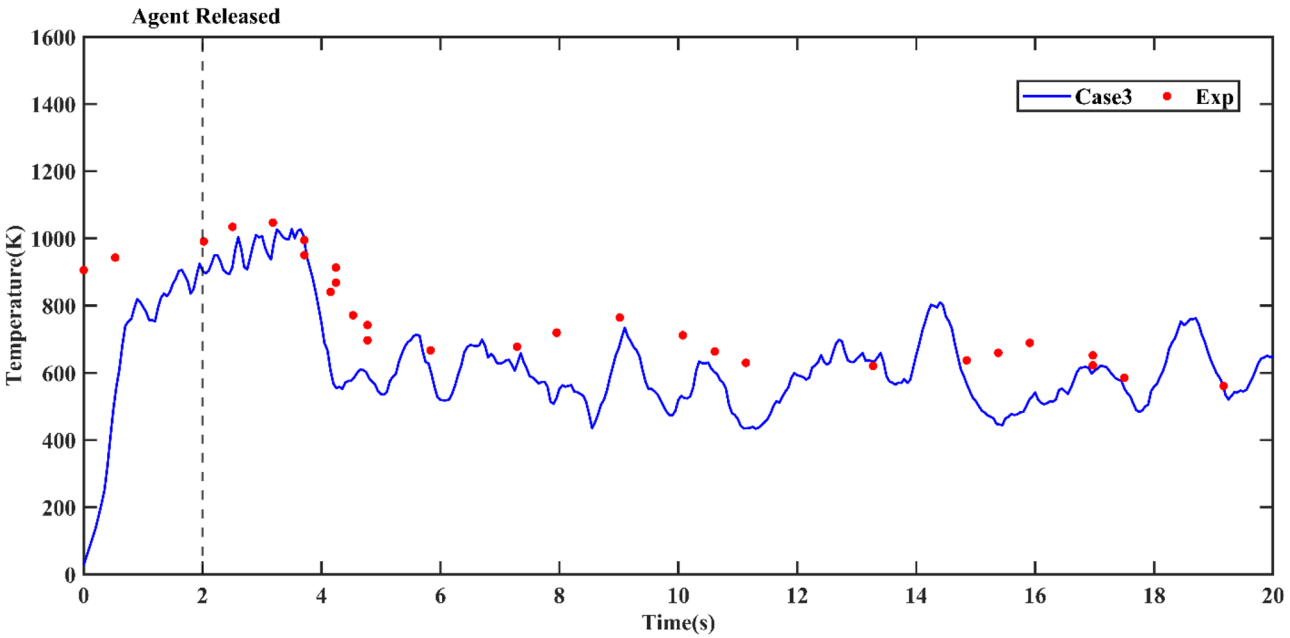


Fig. 7 Validation of temperature profile against the experiment for Case 3 (Baseline model)

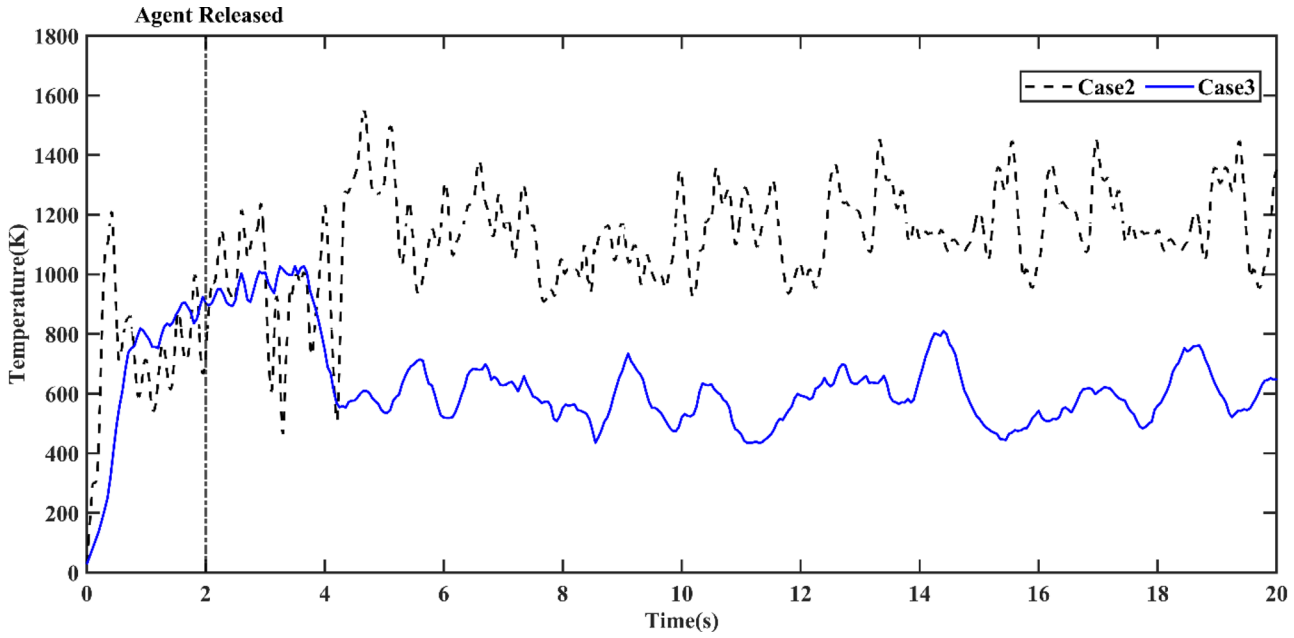


Fig. 8 Variation of the temperature profile in cases 2 and 3

it is suggested that the smaller initial diameter leads to a wider size distribution spectrum that allows a more compact charring formulated above the fuel surface and diminished the contact area between fuel and oxygen. Oppositely, since the larger size (i.e. 850 μm, 1000 μm) of EG particles are able to reach its final volume in a magnitude greater than other cases by adopting the same expansion rate, where the larger particle surface area leads to a greater heat transfer rate between particle and flame plume, particles with large diameter also resulted in a greater drag force that extends the contact time between particles and fire. Nonetheless, it can be significantly observed that the smaller size of EG has resulted in a more advantageous suppression performance than the larger sizes.

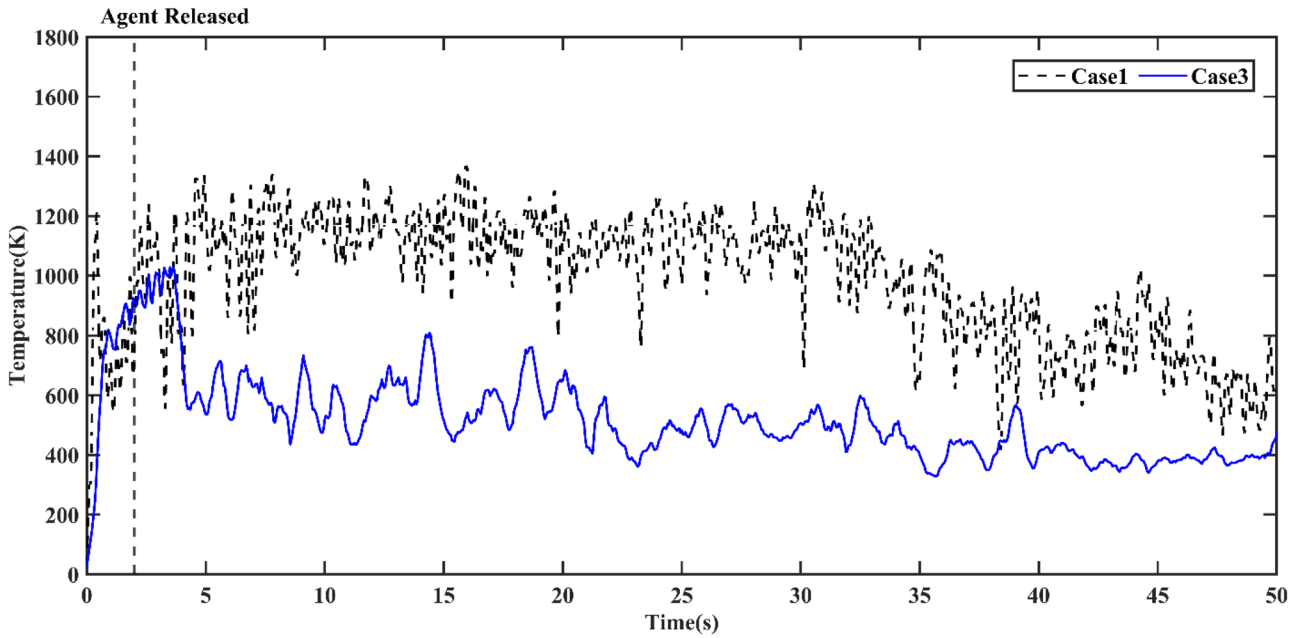


Fig. 9 The comparison of temperature profile between cases 1 and 3

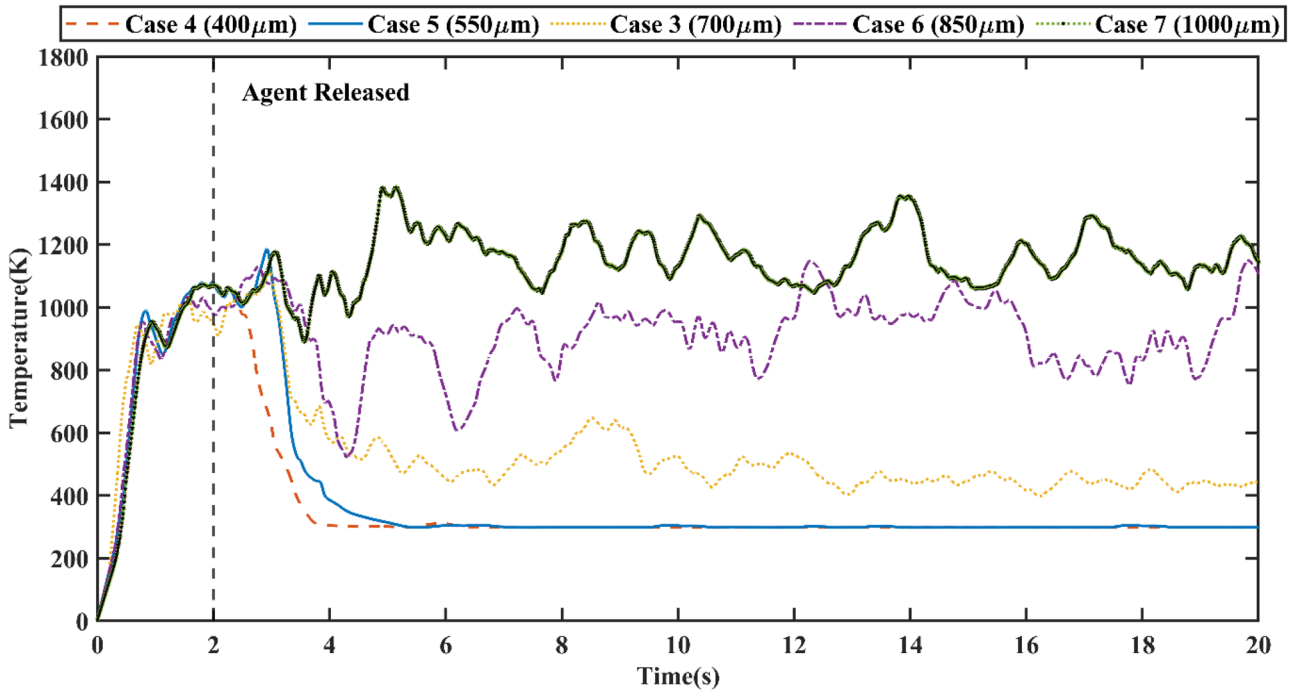


Fig. 10 Temperature profile extracted from the thermocouple in cases 3 to 7

4.5 In-depth particle volume and temperature analysis over the time spectrum

To accumulate the physical characteristics of each individual EG particle, the fuel surface is configurated as a sampling plane and it is used to track the physical parameters of EG particles across the fuel surface, such as temperature and volume. The expandable particles have been sampling since the simulation initiated, the particles were sampled at their arrivals on the fuel surface, hence the particle's information was mainly extracted within the injection time window. Figure 11 presents the volume of particle arrived on the fuel surface versus time and temperature of the suppression period in case 3, it is noticeable that for a time-dependent profile, the particle size fluctuated due to the complex fluid mixture interacting behaviour (i.e. turbulence, combustion). Nevertheless, it is observed that the expansion function is well-coupled with the temperature fluctuation throughout the suppression, the highest expansion ratio has been reached at the beginning of the particles' arrival due to the high-temperature flame at about 1000 K. Afterwards, the volume of the particles in later arrivals have gradually decreased since the flame was being suppressed by the prior particles, where the lower temperature resulted in poorer expansion effect. To further illustrate this phenomenon, the time history of average particle volumes arriving on the fuel surface in both cases 4 and 7 were compared in Fig. 12. Distinct volume change histories were found for different initial EG particle sizes. This distinct behaviour can also be ascribed to the different suppression efficiency of the corresponding EGs. It can be seen that in case 4, the particle volume stays unchanged after around 3 s, this can be attributed to the rapid suppression of the fire. With fire being suppressed, EG particles cannot absorb more heat from fire to achieve expansion. Oppositely, as the EG particles with a larger diameter in case 7 failed to suppress the fire effectively, the volume of EG remains expanded during the suppression. It is also discovered that the smaller EG particles tend to expand to a wider size distribution spectrum.

Since the char layer on the fuel surface is able to exclude oxygen from the fuel, the expansion rate is a key parameter that governing the suppression performance of powder agents. Besides char formation, the expanded volume in the heating process would increase the surface area of the particle, which would raise the rate of heat transfer. To further verify the expansion mechanism triggered by heat, Fig. 13 reveals the expanded volume between simulation and experiments against temperature. The expanded volume of sampled particles is also scattered to demonstrate the convergence of the expansion function. Although few variations in the expanded volume are observed in a certain range of temperature, the expansion trend of the simulation is still in good agreement with the experiments.

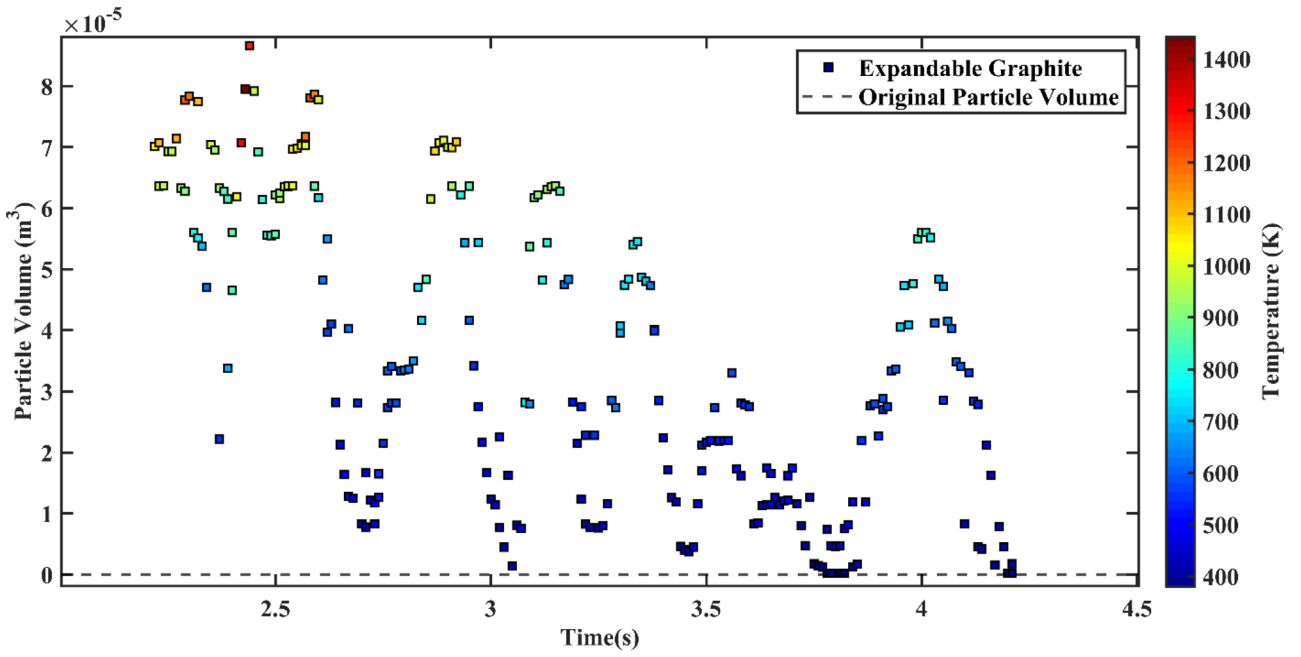


Fig. 11 Particle volume versus time and temperature of the suppression period in case 3

4.6 Fire suppression stages and eg suppression mechanisms

Figure 14 and Fig. 15 reveals the temperature contour over time demonstrating the suppression event in case 3 and case 7, which presented the flame suppression at the corresponding instant. In case 3, a flame suppression was observed between t = 3.2 s and t = 4.2 s, where the temperature was continuously suppressed under the minimum auto-ignition temperature at about 900 K [56]. While in case 7, the 1000 µm EG did not conduct any efficient suppression, the fire remains at approximately 1000 K after the application of

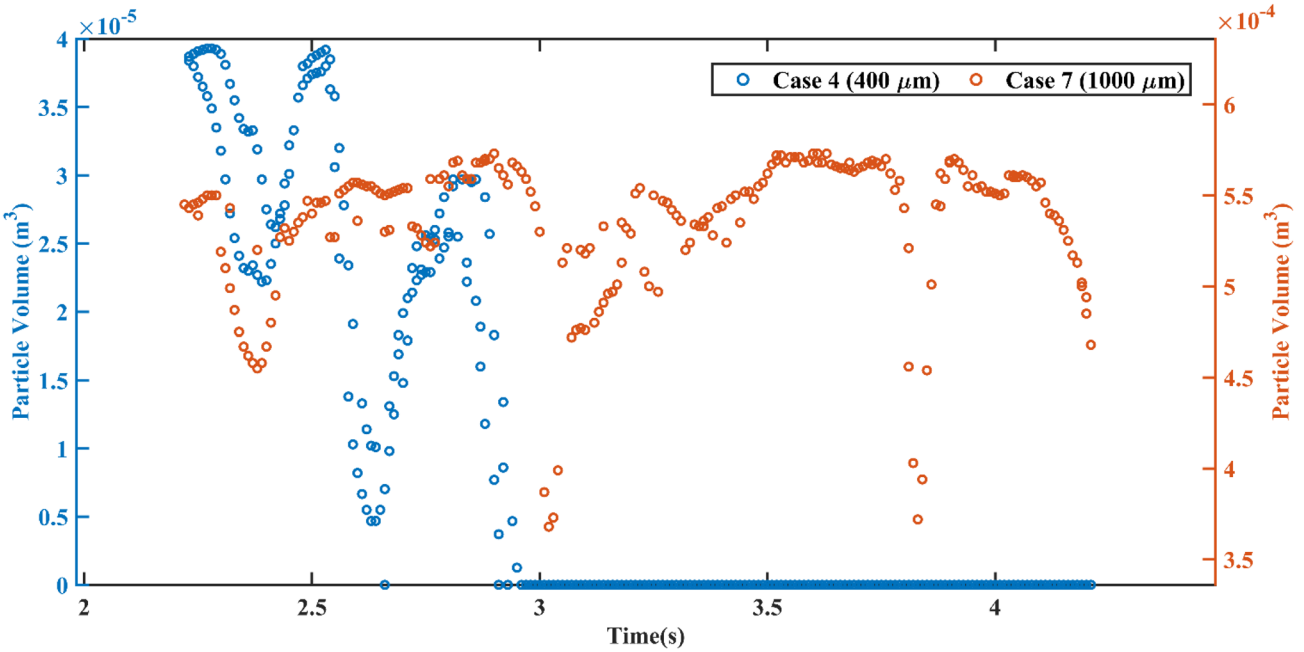


Fig. 12 Particle volume versus time throughout the suppression period in case 4 and 5

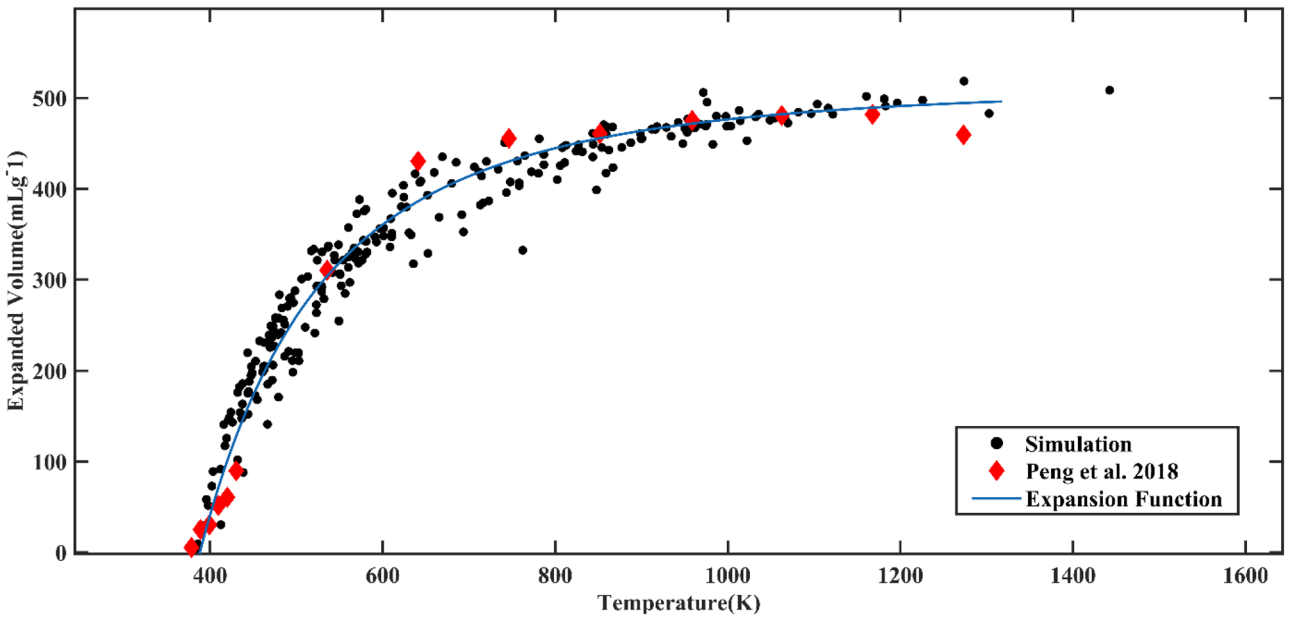


Fig. 13 Particle volume and area versus temperature in case 3

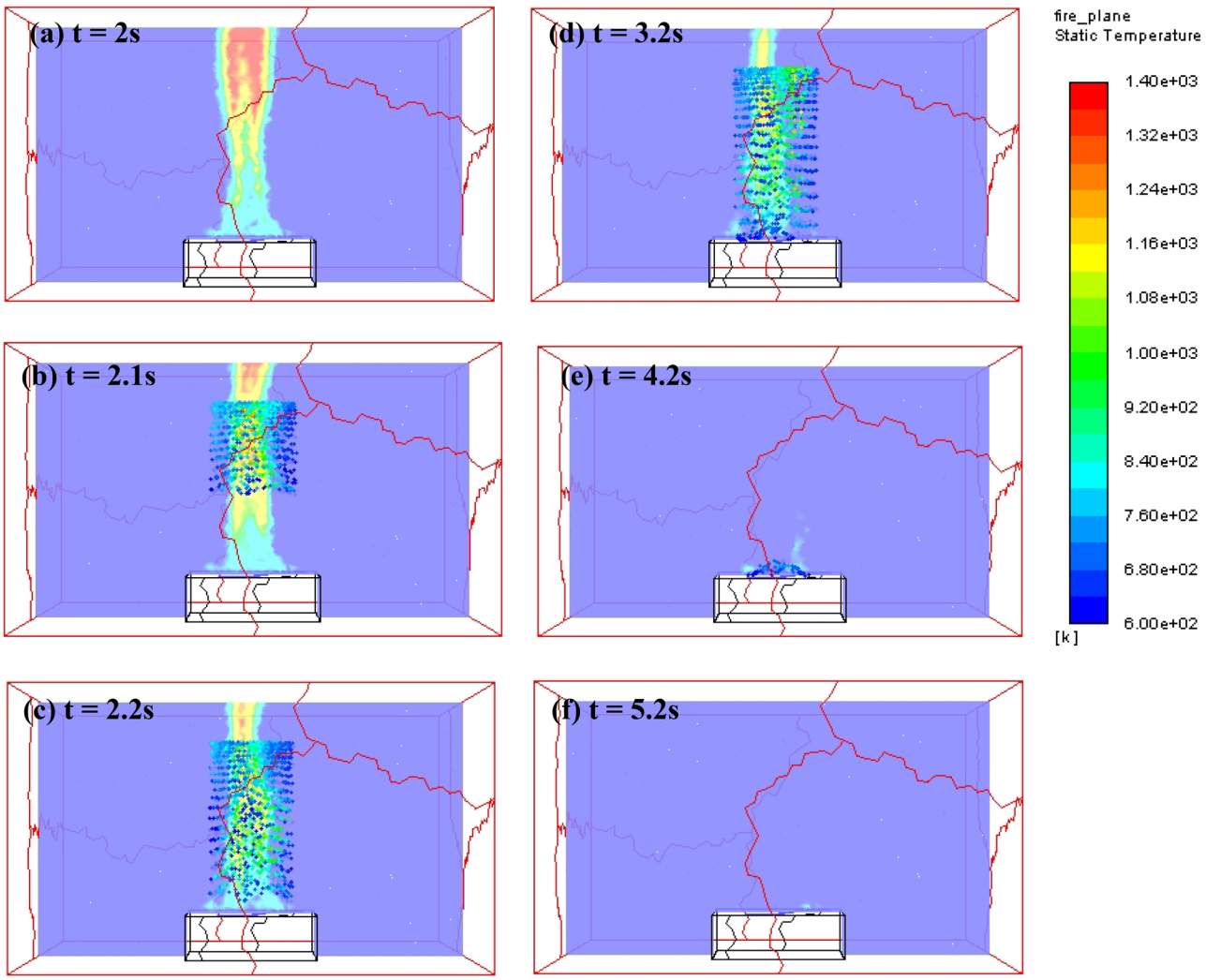


Fig. 14 Temperature contour over time demonstrating the suppression event in case 3

agents, to understand performance differences between case 3 and 7, it is vital to investigate and analyse the suppression mechanism of EG. The suppression mechanism of the EG can be analysed in three approaches: Firstly, the expansion phenomenon of the EG is initiated by the overcoming of Van der Waals force between graphene layers, thus in the suppression process, the EG conduct an endothermic reaction that absorbs heat from the flame plume to initiate its volume expansion. The suppression performance differences under the same amount of EG and natural graphite between case 2 and case 3 can also be ascribed to EG's endothermic reaction. Moreover, expansion in volume would also increase the contact surface area between particles and flame, which contributes to a greater heat transfer rate. Secondly, the thermal properties of the graphite particle have advantageous its penetrability against the flame plume, the high vaporisation temperature and heat capacity allow the particle to travel to the fuel surface easily compare to water-based or other types of liquid suppressant. Thirdly, EG will form a carbon-based layer on the fuel surface after expanded, the char layer mainly consists of expanded graphite and graphene segments, which creates a barrier effect that the oxygen will be excluded from the fuel surface, hence the reaction rate between fuel and oxygen will be decreased as well. According to the comparison results between the various diameter of EG among case 3 to case 7, the initial size of EG particle has been determined as a key parameter that affects suppression performance, as the smaller size of EG particles would able to form a char layer possesses with wider spectrum in size distribution, where smaller particles could increase the bulk density and occupy the voids between the larger particles, which would further prevent the reaction between fuel and other oxidizers.

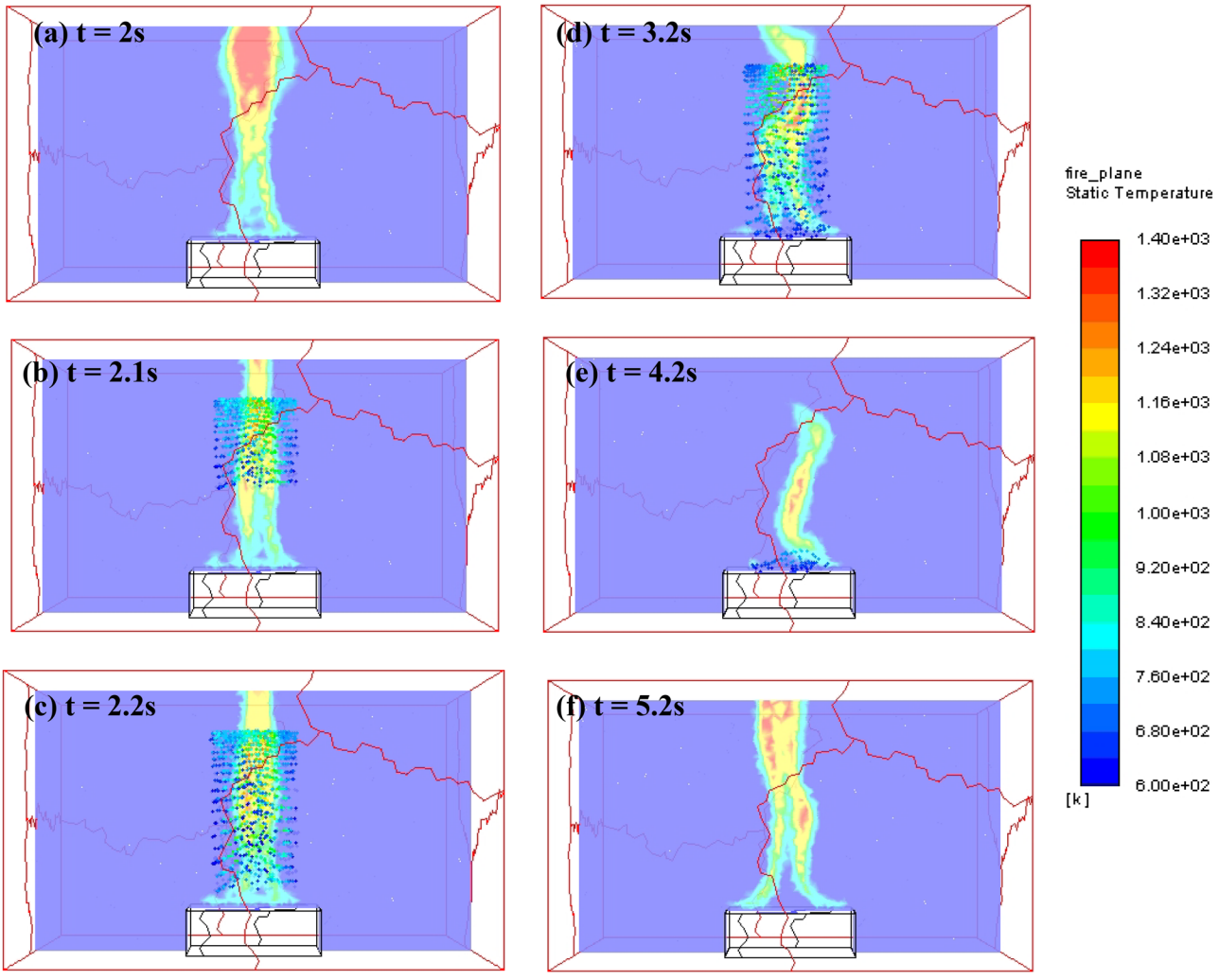


Fig. 15 Temperature contour over time demonstrating the suppression event in case 7

5 Conclusions

In this article, a predictive EG suppression model has been proposed, the model was verified and validated based on conducted experiments. In order to replicate the thermal properties of the EG, such as volume expansion and residual consideration, multiple user-defined functions were adopted in the simulation. The temperature-dependent expansion rate is compiled into the DPM model according to conducted material tests, a fuel surface area reduction method has also been proposed to estimate the char formation rate. To enhance the wall effect on the turbulence closure and associate its interaction towards the fluid mixture and combustion process, the WALE SGS model was employed and found to be effective for this case study. By implementing the proposed in-house UDF model, the expansion effect of EG was successfully modelled and the heat and mass exchange among suppressant/mixture is coupled. This allows the capability of studying particle-based suppression system on metal-based fire (i.e. lithium-ion battery system).

Throughout the investigation, both temperature profile and the expansion rate were found in good agreement with the conducted experiments' result. Parametric studies were also conducted between natural graphite and various particle size of EG (400 µm—1000 µm), the EG was found to be much effective in fire suppression compared to the same amount of natural graphite. To achieve the same suppression performance, 275 g of natural graphite were consumed compared to 11 g of EG, the enormous mass ratio of 25 have indicated the efficiency gap between natural graphite and EG. Among the different diameter of EG (400 µm—1000 µm), the smaller diameter of EGs (i.e. 400 µm, 550 µm) were determined to be an efficient suppressant against metallic fuel fire, which can be attributed to the wider range of size distribution that further prevents the reaction between fuel and other oxidizers. With limited EG supply at 11 g, the 400 µm EG have demonstrated a rapid extinguishment within 2 s, while the original size of 700 µm took 4 s. On the other hand, the larger diameter of EGs (i.e. 850 µm, 1000 µm) failed to conduct suppression. Based on the results, it has been proven that the expansion rate is essential for accurate predictions of the suppression behaviours and time. The expansion characteristics of EG have contributed to the following suppression mechanisms: (i) The expansion reaction is endothermic that continuously absorbs heat from fire with high vaporisation temperature point; (ii) The surface area of EG particles is increased while being expanded, which leads to a greater heat transfer effect; (iii) The expanded EGs form a pile of char layer on the fuel surface, which exclude oxygen from the fuel and thus diminish the reaction rate of combustion. Therefore, EG is considered to be a potential suppression agent in metal fire scenarios, owing to its heat extraction efficiency, chemical stability and the ability of oxygen insulation.

Acknowledgements All financial and technical support are deeply appreciated by the authors. This research was sponsored by the Australian Research Council (ARC Industrial Transformation Training Centre IC170100032). The authors declare no conflict of interest.

References

1. Sakintuna B, Lamari-Darkrim F, Hirscher M (2007) "Metal hydride materials for solid hydrogen storage: A review," Intern J Hydro Energy 32(9):1121–1140. 2007/06/01. https://doi.org/10.1016/j.ijhydene.2006.11.022
2. Association NFP (2006) Standard for Combustible Metals. National Fire Protection Association.
3. Safety CfCP (1995) Guidelines for safe storage and handling of reactive materials. Am Ins Chem Eng.
4. Handbook D (1994) "Primer on spontaneous heating and pyrophoricity," US Department of energy, Washington, DC, 20585
5. Fluegeman C, Hilton T, Moder KP, Stankovich R (2005) Development of detailed action plans in the event of a sodium hydride spill/fire. Process Saf Prog 24(2):86–90
6. Huo Y, Zhang ZG, Zou GW (2020) "Experimental study on the thermal flow characteristics of a columnar sodium fire affected by a small amount of fire extinguishing powder in a cylindrical confined space." Appl Thermal Eng 170:114983. 2020/04/01/. https://doi.org/10.1016/j.applthermaleng.2020.114983
7. Lin S, Dong L, Zhang J, Lu H (2016) "Room-Temperature Intercalation and ~1000-Fold Chemical Expansion for Scalable Preparation of High-Quality Graphene." Chem Mater 28(7):2138–2146 2016/04/12. https://doi.org/10.1021/acs.chemmater.5b05043
8. Cai M, Thorpe D, Adamson DH, Schniepp HC (2012) "Methods of graphite exfoliation," J Mater Chem. 22(48):24992–25002. https://doi.org/10.1039/C2JM34517J
9. Peng T, Liu B, Gao X, Luo L, Sun H (2018) Preparation, quantitative surface analysis, intercalation characteristics and industrial implications of low temperature expandable graphite. Appl Surf Sci 444:800–810. https://doi.org/10.1016/j.apsusc.2018.03.089
10. Zhan H, Zhang Y, Bell JM, Gu Y (2015) "Suppressed Thermal Conductivity of Bilayer Graphene with Vacancy-Initiated Linkages." J Physical Chem C 119(4):1748–1752. 2015/01/29. https://doi.org/10.1021/jp5117905
11. Pang XY, Song MK, TIAN Y, Duan MW (2012) "Preparation of high dilatability expandable graphite and its flame retardancy for lldpe." J Chilean Chem Soc 57(3)
12. Zhang Z, Li D, Xu M, Li B (2020) "Synthesis of a novel phosphorus and nitrogen-containing flame retardant and its application in rigid polyurethane foam with expandable graphite." Polym Degrad Stability 173:109077
13. Acuña P et al. (2020) "Synergistic effect of expandable graphite and phenylphosphonic-aniline salt on flame retardancy of rigid polyurethane foam" Polym Degrad Stability 179:109274. 2020/09/01. https://doi.org/10.1016/j.polymdegradstab.2020.109274
14. Wang Y, Zhao J, Xiaojing M (2019) "Effect of expandable graphite on polyester resin-based intumescent flame retardant coating," Prog Organic Coat 132:178–183. 2019/07/01. https://doi.org/10.1016/j.porgcoat.2019.03.050
15. Guler T, Tayfun U, Bayramli E, Dogan M (2017) "Effect of expandable graphite on flame retardant, thermal and mechanical properties of thermoplastic polyurethane composites filled with huntite&hydromagnesite mineral." Thermochimica Acta 647:70–80. 2017/01/10. https://doi.org/10.1016/j.tca.2016.12.001
16. Jaszak P (2020) "Modeling of the elastic properties of compressed expanded graphite - A material used in spiral wound gaskets." Intern J Pressure Vessels Piping 187104158. 2020/11/01. https://doi.org/10.1016/j.ijpvp.2020.104158

17. Lin W, Ling Z, Zhang Z, Fang X (2020) "Experimental and numerical investigation of sebacic acid/expanded graphite composite phase change material in a double-spiral coiled heat exchanger." J Energy Storage 32:101849. 2020/12/01. https://doi.org/10.1016/j.est.2020.101849
18. Toyoda M, Nishi Y, Iwashita N,Inagaki M (2003) "Sorption and recovery of heavy oils using exfoliated graphite Part IV: Discussion of high oil sorption of exfoliated graphite." Desalination 151(2):139–144. 2003/01/10. https://doi.org/10.1016/S0011-9164(02)00992-X
19. Li C, Chen X, Shen L, Bao N (2020) "Revisiting the Oxidation of Graphite: Reaction Mechanism, Chemical Stability, and Structure Self-Regulation." ACS Omega 5(7):3397–3404. 2020/02/25. https://doi.org/10.1021/acsomega.9b03633
20. Yuen ACY et al (2018) Numerical study of the development and angular speed of a small-scale fire whirl. J Comput Sci 27:21–34. https://doi.org/10.1016/j.jocs.2018.04.021
21. Chen Q, Chen TBY, Yuen ACY, Wang C, Chan QN, Yeoh GH (2020) "Investigation of door width towards flame tilting behaviours and combustion species in compartment fire scenarios using large eddy simulation." Intern J Heat Mass Trans 150:119373. 2020/04/01. https://doi.org/10.1016/j.ijheatmasstransfer.2020.119373
22. Klein M, Ketterl S, Hasslberger J (2019) Large eddy simulation of multiphase flows using the volume of fluid method: Part 1—Governing equations and a priori analysis. Experimental and Computational Multiphase Flow 1(2):130–144
23. Liu H et al (2020) "Critical assessment on operating water droplet sizes for fire sprinkler and water mist systems." J Build Eng 28:100999. 2020/03/01. https://doi.org/10.1016/j.jobe.2019.100999
24. Liu H et al (2021) "A novel stochastic approach to study water droplet/flame interaction of water mist systems," Num Heat Trans, Part A: Applications 1–27. https://doi.org/10.1080/10407782.2021.1872272
25. Li YZ, Ingason H (2018) "Influence of fire suppression on combustion products in tunnel fires." Fire Safe J 97:96–110. 2018/04/01. https://doi.org/10.1016/j.firesaf.2017.06.011
26. Huaizhong Li AL, Fan J, Yeoh GH, WangJ (2014) On DEM-CFD study of the dynamic characteristics of high speed micro-abrasive air jet.
27. Yan Y, Li X, Ito K (2020) Numerical investigation of indoor particulate contaminant transport using the Eulerian-Eulerian and Eulerian-Lagrangian two-phase flow models. Experimental and computational multiphase flow 2(1):31–40
28. Yuen ACY, Yeoh G, Timchenko V, Cheung S, Chan Q, Chen T (2017) "On the influences of key modelling constants of large eddy simulations for large-scale compartment fires predictions," Intern J Comput Fluid Dynamics 1–14. 08/02 2017. https://doi.org/10.1080/10618562.2017.1357809
29. ACY Y, GH Y, RKK Y, T C (2013) "Numerical Simulation of a Ceiling Jet Fire in a Large Compartment." Procedia Eng 52(0):3–12. https://doi.org/10.1016/j.proeng.2013.02.097
30. Yuen ACY, Yeoh GH (2013) Numerical simulation of an enclosure fire in a large test hall. Comput Thermal Sci 5(6):459–471. https://doi.org/10.1615/ComputThermalScien.2013005954
31. Rehm RG, Baum HR (1978) The equations of motion for thermally driven buoyant flows. Journal of Research of the NBS 83:297–308
32. Knio OM, Najm HN, Wyckoff PS (1999) "A Semi-implicit Numerical Scheme for Reacting Flow: II. Stiff, Operator-Split Formulation," J Comput Phys 154(2):428–467. 1999/09/20. https://doi.org/10.1006/jcph.1999.6322
33. Hinze JO (1975) Turbulence. McGraw-Hill (in English), New York
34. Nicoud F, F. Ducros F (1999) "Subgrid-Scale Stress Modelling Based on the Square of the Velocity Gradient Tensor." Flow, Turbulence and Combustion 62(3):183–200. 1999/09/01. https://doi.org/10.1023/A:1009995426001
35. Wang C et al (2019) "Influence of Eddy-Generation Mechanism on the Characteristic of On-Source Fire Whirl." Appl Sci 9:3989. 09/24/2019. https://doi.org/10.3390/app9193989
36. Yuen ACY, Yeoh GY, Timchenko V, Cheung SCP,Barber TJ (2016) "Importance of detailed chemical kinetics on combustion and soot modelling of ventilated and under-ventilated fires in compartment." Intern J Heat Mass Trans 96171–188. 2016/05/01. https://doi.org/10.1016/j.ijheatmasstransfer.2016.01.026
37. Jones WP (1980) Models for turbulent flows with variable density and combustion. Hemispere Publishing Corp, United States
38. Morsi SA, Alexander AJ (1972) An investigation of particle trajectories in two-phase flow systems. J Fluid Mech 55(2):193–208. https://doi.org/10.1017/S0022112072001806
39. ANSYS Inc. "ANSYS Fluent Theory Guide." Accessed.
40. Clarke JT, Fox BR (1969) Rate and Heat of Vaporization of Graphite above 3000°K. J Chem Phys 51(8):3231–3240. https://doi.org/10.1063/1.1672500
41. Marshall AL, Norton FJ (1933) "Vapor pressure and heat of vaporization of graphite." J Am Chem Soc 1:431–432. 1933/01/01. https://doi.org/10.1021/ja01328a513
42. Pang X, Tian Y, Duan M, Zhai M (2013) "Preparation of low initial expansion temperature expandable graphite and its flame retardancy for LLDPE." Central Euro J Chem 11. 06/01/2013. https://doi.org/10.2478/s11532-013-0227-2
43. Chung DDL (1987) Exfoliation of graphite. J Mater Sci 22:4190–4198
44. Cai M, Thorpe D, Adamson DH, Schniepp HC (2012) Methods of graphite exfoliation. J Mater Chem 22:24992–25002
45. McAllister MJ et al (2007) Single Sheet Functionalized Graphene by Oxidation and Thermal Expansion of Graphite. Chem Mater 19:4396–4404
46. Pang X, Tian Y, Duan M, Zhai M (2013) “Preparation of low initial expansion temperature expandable graphite and its flame retardancy for LLDPE,” (in English). Open Chem 11(6):953. https://doi.org/10.2478/s11532-013-0227-2
47. Vovchenko LL, Matzui LY, Kulichenko AA (2007) "Thermal characterization of expanded graphite and its composites," Inorganic Mater 43(6):597–601. 2007/06/01. https://doi.org/10.1134/S0020168507060088
48. Vafajoo L, Khorasheh F, Nakhjavani M, Fattahi M (2014) Kinetic parameters optimization and modeling of catalytic dehydrogenation of heavy paraffins to olefins. Pet Sci Technol 32(7):813–820
49. Ni x, Zheng 2 (2020) "Extinguishment of sodium fires with Graphite@Stearate core-shell structured particles." Fire Safe J 111. https://doi.org/10.1016/j.firesaf.2019.102933
50. Zhang T, Bi M, Jiang H, Gao W (2020) Suppression of aluminum dust explosions by expandable graphite. Powder Technol 366:52–62. https://doi.org/10.1016/j.powtec.2020.02.053
51. Focke WW, Badenhorst H, Mhike W, Kruger HJ, Lombaard D (2014) "Characterization of commercial expandable graphite fire retardants." Thermochimica Acta 584:8–16. 2014/05/20. https://doi.org/10.1016/j.tca.2014.03.021
52. DiNenno PJ (2008) "SFPE handbook of fire protection engineering.
53. Staple W (1975) The influence of size distribution on the bulk density of uniformly packed glass particles. Soil Sci Soc Am J 39(3):404–408
54. Samal P, Newkirk J (2015) "Powder metallurgy methods and applications," ASM handbook of powder metallurgy 7
55. Zhang S (2017) "Relationship between particle size distribution and porosity in dump leaching." University of British Columbia.
56. Robinson C, Smith DB (1984) "The auto-ignition temperature of methane." J Hazard Mater 8(3):199–203. 1984/01/01. https://doi.org/10.1016/0304-3894(84)85001-3